Drivers of Atmospheric and Oceanic Surface Temperature Variance: A Frequency Domain Approach

PAIGE E. MARTIN,[a] BRIAN K. ARBIC,[a] AND ANDREW MCC. HOGG[b]

[a] *Department of Earth and Environmental Sciences, University of Michigan, Ann Arbor, Michigan*
[b] *Research School of Earth Sciences and ARC Centre of Excellence for Climate Extremes, Australian National University, Canberra, Australian Capital Territory, Australia*

(Manuscript received 15 July 2020, in final form 4 February 2021)

ABSTRACT: Ocean–atmosphere coupling modifies the variability of Earth's climate over a wide range of time scales. However, attribution of the processes that generate this variability remains an outstanding problem. In this article, air–sea coupling is investigated in an eddy-resolving, medium-complexity, idealized ocean–atmosphere model. The model is run in three configurations: fully coupled, partially coupled (where the effect of the ocean geostrophic velocity on the sea surface temperature field is minimal), and atmosphere-only. A surface boundary layer temperature variance budget analysis computed in the frequency domain is shown to be a powerful tool for studying air–sea interactions, as it differentiates the relative contributions to the variability in the temperature field from each process across a range of time scales (from daily to multidecadal). This method compares terms in the ocean and atmosphere across the different model configurations to infer the underlying mechanisms driving temperature variability. Horizontal advection plays a dominant role in driving temperature variance in both the ocean and the atmosphere, particularly at time scales shorter than annual. At longer time scales, the temperature variance is dominated by strong coupling between atmosphere and ocean. Furthermore, the Ekman transport contribution to the ocean's horizontal advection is found to underlie the low-frequency behavior in the atmosphere. The ocean geostrophic eddy field is an important driver of ocean variability across all frequencies and is reflected in the atmospheric variability in the western boundary current separation region at longer time scales.

KEYWORDS: Air-sea interaction; Heat budgets/fluxes; Surface temperature; Fourier analysis; Quasigeostrophic models; Climate variability

1. Introduction

Ocean–atmosphere interaction is an important component of Earth's climate system. Heat exchanged at the interface of the ocean and atmosphere is one of the key processes controlling climate variability. The communication between the ocean and atmosphere is complicated by the multitude and time dependence of processes contributing to variability, as well as the inherently coupled nature of the climate system. In this study, we examine the processes involved in surface temperature variability in the ocean and atmosphere and the time scales at which each of these processes act.

It is well established that oceanic and atmospheric dynamics have preferred time scales. The classical view is that the slow-moving ocean integrates the atmosphere's high-frequency (interannual and shorter) dynamics into low-frequency (decadal and longer) variability (Bjerknes 1964; Hasselmann 1976; Frankignoul and Hasselmann 1977). Over the decades, many studies (e.g., Barsugli and Battisti 1998; Sutton and Allen 1997; Kushnir et al. 2002; Bishop et al. 2017) have built upon this paradigm, which remains the basis of our understanding of air–sea coupling.

Air–sea interaction has been diagnosed in the literature using a number of different methods in recent years. For instance, lagged correlation between sea surface temperature (SST) and surface heat flux has been used (e.g., Gulev et al. 2013; Bishop et al. 2017) to determine the time scales at which SST and heat fluxes are positively correlated (interpreted as the atmospheric heat fluxes driving ocean SST dynamics) or negatively correlated (indicating ocean-driven behavior). Other studies (Buckley et al. 2014, 2015; Small et al. 2020) calculate the upper-ocean heat budget (the temperature field integrated over a certain depth) and use correlation techniques to determine the relative contributions of each term to the heat budget. Among their findings, Buckley et al. (2015) suggest that the surface heat fluxes may not be entirely atmosphere-driven, indicating the need to better understand the driving mechanisms of each term contributing to temperature variability.

More specifically, Buckley et al. (2014, 2015) and Small et al. (2020) decompose the upper-ocean heat budget into components (including advection, Ekman, and surface heat flux contributions) in regional ocean and global climate models. Their results show that the processes involved in air–sea coupling vary widely by region and time scale. Through employment of spectral analysis in the frequency domain on a low-resolution (1°) ocean model, Buckley et al. (2014, 2015) find that local atmospheric forcing drives much of the upper-ocean heat content across the North Atlantic basin. Over the Gulf Stream atmospheric forcing dominates only on subannual scales, while geostrophic advection plays a dominant role at interannual scales. This time scale dependence aligns with results from Bishop et al. (2017), who determine that the ocean influence on SST variability increases with time scale, but decreases with spatial scale. Small et al. (2020)

Corresponding author: Paige E. Martin, paigemar@umich.edu

DOI: 10.1175/JCLI-D-20-0557.1

use a regression method on a high-resolution (0.1° ocean and 0.25° atmosphere) eddying coupled model to compare the contributions from terms in the upper-ocean heat budget. They find that, at monthly time scales, ocean-driven processes play a substantial role in driving variability of temperature anomalies via advection, particularly (but not exclusively) in the strongly eddying regions of the ocean (western boundary currents). We note that all three of these studies use monthly output for their analyses; with a focus on both oceanic and atmospheric variability across time scales, we use daily output in this work and can thus resolve variability at shorter time scales.

Recent evidence suggests that ocean eddies play a significant role in air–sea interactions, impacting both oceanic and atmospheric dynamics. For instance, Chelton et al. (2004), Minobe et al. (2008), and Small et al. (2008) (and references therein) detail many ways in which ocean eddies impact the atmospheric boundary layer and the resulting feedback into the ocean. These eddy-driven air–sea feedbacks are especially significant in the North Atlantic due to the energetic eddy activity in the Gulf Stream (Kirtman et al. 2012). For example, eddy-driven feedback with the atmosphere is crucial in setting the position and separation of the Gulf Stream (Renault et al. 2016). The importance of eddy contributions to temperature variability is further shown by Kirtman et al. (2017), who demonstrate the large, nonlinear effect that eddies have on the ocean SST variance. There is also evidence that ocean eddies can influence atmospheric variability beyond the atmospheric boundary layer (Deremble et al. 2012; Lambaerts et al. 2013), further indicating the need to study high-resolution, fully coupled ocean–atmosphere models.

The dependence of SST variance on mechanical air–sea coupling is explored by Larson et al. (2018). They compare two global 1° ocean–atmosphere model runs, one with full coupling and one that is mechanically decoupled; in the latter a climatological, rather than a dynamic, atmospheric wind stress is passed to the ocean. Through employment of this partial coupling, Larson et al. (2018) are able to determine that temperature variance is decreased significantly in the midlatitudes in the absence of Ekman processes. In the current study, we also make use of partial coupling, but in a different configuration (explained below) that highlights the effect of ocean mesoscale eddies on both ocean and atmosphere surface temperature variance.

Building upon earlier work (Hayashi 1980; Sheng and Hayashi 1990), a number of recent studies (Arbic et al. 2012, 2014; Sérazin et al. 2018; O'Rourke et al. 2018; Martin et al. 2020) have used a frequency-domain technique to study energy budgets. They have all shown that this spectral energy budget method is a powerful tool in deciphering the contribution of nonlinear advection and other terms to variability at different time scales. Most of the recent studies cited above focus on ocean models and observations. Martin et al. (2020) employ the technique to identify the processes that deposit energy into, or extract energy from, both the ocean and atmosphere at specific time scales within the Quasi-Geostrophic Coupled Model (Q-GCM; Hogg et al. 2003). Overall, Martin et al. (2020) find that intrinsically driven kinetic energy advection creates variability in both the ocean and atmosphere at time scales longer than monthly in the atmosphere, and longer than interannual in the ocean. They also identify oceanic regions with distinct patterns of variability, notably the western boundary current separation region.

Hochet et al. (2020) use a similar frequency-domain technique to diagnose the depth-integrated temperature variance budget (in contrast to the energy budget) in an idealized eddy-permitting primitive equation ocean model. They find that horizontal advection drives a forward cascade toward higher frequencies in the depth-integrated temperature variance budget, consistent with expectations from previous work (e.g., Arbic et al. 2012, 2014) on the cascade of available potential energy in the quasigeostrophic limit, in which available potential energy is equivalent to temperature variance. Hochet et al. (2020) use the frequency-domain technique to supplement interpretations of low-frequency (multidecadal) variability of the overturning circulation. In their eddying model the eddies serve to damp low-frequency temperature variance and transfer variance to high frequencies.

With particular interest in understanding the time scales of variability, in this paper we transform the surface temperature variance budgets of the medium-complexity Q-GCM into the frequency domain. This technique disentangles the processes that drive temperature variability via surface temperature variance budgets calculated in the ocean, as well as the atmosphere. Several of the aforementioned studies (Buckley et al. 2014, 2015; Larson et al. 2018; Small et al. 2020) isolate the Ekman transport contribution to the advection in their models. Here, we separate the Ekman transport contribution and go a step further by running both an atmosphere-only and a "partially coupled" model experiment in which the direct ocean geostrophic contribution to advection is removed from the ocean mixed layer leaving only Ekman-driven advection (noting that the stress term depends weakly on geostrophic dynamics). The partially coupled configuration is specifically designed to change only this one feature of Q-GCM, while all other aspects of the coupled run remain intact. By removing the direct effect of geostrophic eddy advection on the ocean mixed layer we can determine the role that ocean eddies, as well as Ekman transport processes, play in SST variability. As mentioned previously, the idea of partial coupling to identify underlying mechanisms of variability is not new (e.g., Hogg et al. 2006; Larson et al. 2018; Liu and Di Lorenzo 2018), but we are, to our knowledge, the first to use this particular coupling setup to investigate surface temperature fields.

Using the frequency-domain temperature variance budget analysis in conjunction with partial coupling provides key insight into the underlying mechanisms driving variability in Q-GCM across a range of time scales. In the next section we describe the model setup and the coupling configurations. The frequency-domain temperature variance equations are outlined in section 3. Section 4 presents the results of the temperature variance spectra and budgets in both the ocean and atmosphere. Finally, we discuss the results and conclude in section 5.

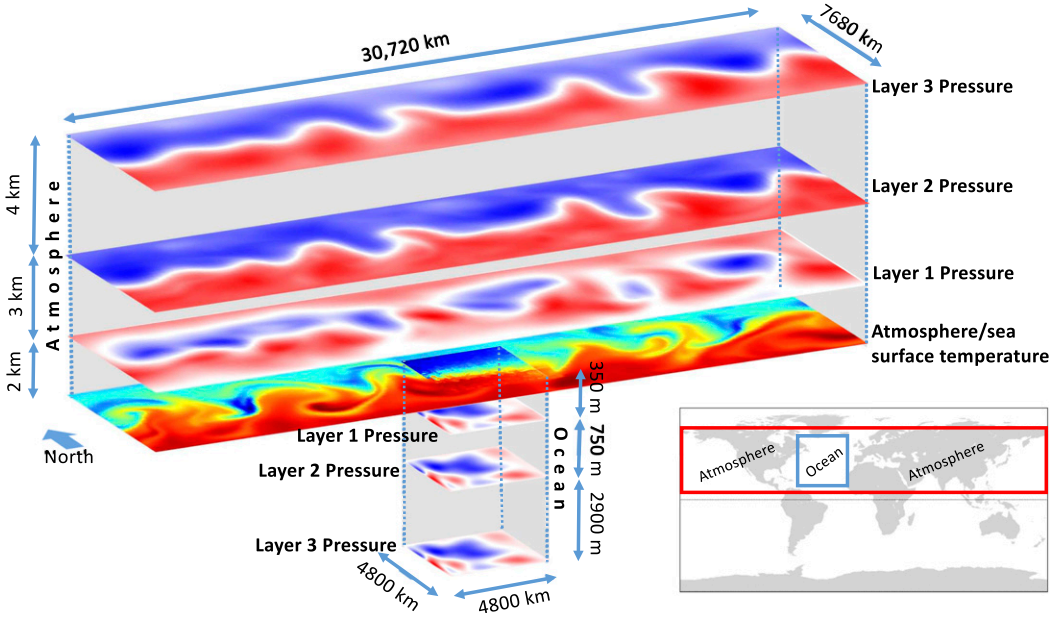

FIG. 1. Schematic of Q-GCM. Snapshots of layer pressure are shown for the quasigeostrophic layers in the atmosphere and ocean. Snapshots of atmosphere and sea surface temperature are shown at the ocean–atmosphere interface. Note that the vertical axis is not drawn to scale. The map in the bottom right displays the rough geographical location of the region that this Q-GCM ocean (outlined in blue) and atmosphere (outlined in red) simulation is meant to idealize. The black dotted line indicates the equator.

2. Quasi-Geostrophic Coupled Model

a. Model setup

We use the Quasi-Geostrophic Coupled Model v1.5.0 (Q-GCM; Hogg et al. 2003, 2014) consisting of a box ocean coupled to a reentrant channel atmosphere. The model (shown schematically in Fig. 1) represents the northern midlatitudes, with the ocean tuned to mimic the North Atlantic with a middle latitude of 40°N. There are three quasigeostrophic layers in both the ocean and atmosphere, separated by ageostrophic mixed layers at the interface of both fluids (i.e., the ocean and the atmosphere) in order to allow for the air–sea coupling in the model via vertical heat fluxes and momentum exchange. The model has no bottom topography, is spun up from rest for 50 years before analysis is undertaken, and is driven only by a temporally constant, latitudinally varying influx of solar shortwave radiation. The model generates daily output, and diurnal and seasonal variation are not present in the model.

In the current study, we focus on the mixed layers in the model, where the air–sea coupling takes place. The atmosphere (denoted by superscript a) mixed layer (denoted by subscript m) temperature field (T) evolves in time according to the following:

$$\frac{\partial}{\partial t}({}^{a}T_m) = \underbrace{-({}^{a}u_m\,{}^{a}T_m)_x - ({}^{a}v_m\,{}^{a}T_m)_y}_{\text{horizontal temperature advection}} - \overbrace{\frac{{}^{a}w_{\text{ek}}\,{}^{a}T_m}{{}^{a}h_m}}^{\text{vertical temperature advection}} - \underbrace{\frac{F_s}{{}^{a}\rho^{a}C_p\,{}^{a}h_m}}_{\text{solar radiation over land}} + \underbrace{\frac{F_\lambda}{{}^{a}\rho^{a}C_p\,{}^{a}h_m}}_{\text{sensible and latent heat flux}} + \underbrace{\frac{F_0^{\uparrow}+F_m^{\downarrow}}{{}^{a}\rho^{a}C_p\,{}^{a}h_m}}_{\text{heat flux from ocean and land}}$$

$$\underbrace{\qquad\qquad\qquad\qquad\qquad\qquad\qquad\qquad\qquad\qquad\qquad\qquad}_{\text{surface heat fluxes}}$$

$$- \overbrace{\frac{F_m}{{}^{a}\rho^{a}C_p\,{}^{a}h_m}}^{\text{heat fluxes to layer 1}} + \underbrace{{}^{a}K_2\nabla_H^2\,{}^{a}T_m - {}^{a}K_4\nabla_H^4\,{}^{a}T_m}_{\text{diffusion}}. \tag{1}$$

TABLE 1. Q-GCM parameters.

Parameter	Ocean value	Atmosphere value
Basin dimensions	4800 km × 4800 km	30 720 km × 7680 km
Number of grid points	960 × 960	384 × 96
Horizontal grid spacing	5 km	80 km
Approximate latitude and longitude extent	18°–62°N, 10°–70°W	5°–75°N, 180°W–180°E
Atmosphere indices over ocean	–	x: 163–223, y: 19–79
Layer thicknesses (H_1, H_2, H_3)	350, 750, 2900 m	2000, 3000, 4000 m
Mixed layer thicknesses (H_m)	100 m	1000 m
Time step	9 min	3 min
Mean Coriolis parameter at 40°N (f_0)	$9.374\,56 \times 10^{-5}\,s^{-1}$	$9.374\,56 \times 10^{-5}\,s^{-1}$
y derivative of Coriolis parameter (β)	$1.753\,60 \times 10^{-11}\,m^{-1}\,s^{-1}$	$1.753\,60 \times 10^{-11}\,m^{-1}\,s^{-1}$
Density (ρ)	$1000\,kg\,m^{-3}$	$1\,kg\,m^{-3}$
Heat capacity (C_p)	$1 \times 10^3\,J\,kg^{-1}\,K^{-1}$	$4 \times 10^3\,J\,kg^{-1}\,K^{-1}$
Layer temperatures (T_1, T_2, T_3)	287, 282, 276 K	330, 340, 350 K
Temperature diffusion coefficients (K_2, K_4)	200, $2 \times 10^9\,m^4\,s^{-1}$	2.5×10^4, $2 \times 10^{14}\,m^4\,s^{-1}$
Mean radiative forcing ($\overline{F_S}$)	–	$-220\,W\,m^{-2}$
Radiation perturbation magnitude (F_S')	–	$80\,W\,m^{-2}$
Adiabatic lapse rate (γ)	–	$1 \times 10^{-2}\,K\,m^{-1}$
Bottom Ekman layer thickness (δ_{ek})	1 m	–
Reduced gravities (g_1', g_2')	0.015, 0.0075 $m\,s^{-2}$	1.2, 0.4 $m\,s^{-2}$
Biharmonic viscosity (A_4)	$2 \times 10^9\,m^4\,s^{-1}$	$1.5 \times 10^{14}\,m^4\,s^{-1}$
Mixed boundary condition parameter (α_{bc})	0.2	1.0
Drag coefficient (C_D)	1.3×10^{-3}	1.3×10^{-3}

The ocean (denoted by superscript o) mixed layer temperature evolution equation is

$$\frac{\partial}{\partial t}({}^oT_m) = \underbrace{-({}^ou_m\,{}^oT_m)_x - ({}^ov_m\,{}^oT_m)_y}_{\text{horizontal temperature advection}} + \overbrace{\frac{{}^ow_{ek}\,{}^oT_m}{{}^oH_m}}^{\text{vertical temperature advection}} + \overbrace{\frac{F_m^{e+}}{{}^o\rho\,{}^oC_p\,{}^oH_m}}^{\text{entrainment heat flux}} - \underbrace{\underbrace{\frac{F_\lambda}{{}^o\rho\,{}^oC_p\,{}^oH_m}}_{\text{sensible and latent heat flux}} - \underbrace{\frac{F_0^{\uparrow} + F_m^{\downarrow}}{{}^o\rho\,{}^oC_p\,{}^oH_m}}_{\text{radiative heat flux}}}_{\text{surface heat fluxes}}$$

$$- \overbrace{\frac{F_s}{{}^o\rho\,{}^oC_p\,{}^oH_m}}^{\text{solar radiation}} + \underbrace{{}^oK_2\nabla_H^2\,{}^oT_m - {}^oK_4\nabla_H^4\,{}^oT_m}_{\text{diffusion}}. \tag{2}$$

Mixed layer velocities are written as u_m (eastward direction) and v_m (northward direction). The Ekman velocity w_{ek} is defined in both fluids as proportional to the vertical component of the curl of the wind stress τ ($\nabla \times \tau$)/f_0, and the formulation of τ is given in the appendix. The brackets in the above equations are used to specify our naming conventions for each term throughout the paper; for instance, we will refer to the heat flux terms as either sensible/latent or radiative. Due to incompressibility constraints, the mixed layer height in the atmosphere (^ah_m) varies in time, unlike its counterpart in the ocean, which remains constant $^oH_m = 100$ m. We run the model with a horizontal resolution of 5 km in the ocean and 80 km in the atmosphere; there are roughly six grid cells per 30-km ocean deformation radius, and we thus consider the model to resolve ocean mesoscale eddies. A bilinear interpolation scheme is used to interpolate quantities between the oceanic and atmospheric grids. Specific formulations of the variable mixed layer height and heat flux terms can be found in the appendix. The remaining variables and constants are described in Table 1. For the governing equations of the quasigeostrophic layers, we refer the reader to the Q-GCM user guide (Hogg et al. 2014).

b. Model configurations

To better understand the mechanisms underlying temperature variability in Q-GCM, three different configurations of the model are run: fully coupled (FC), partially coupled (PC), and atmosphere-only (AT). The difference between FC and PC lies in the ocean's mixed layer velocity formulation. In FC, the ocean's mixed layer velocities are given by the sum of the first

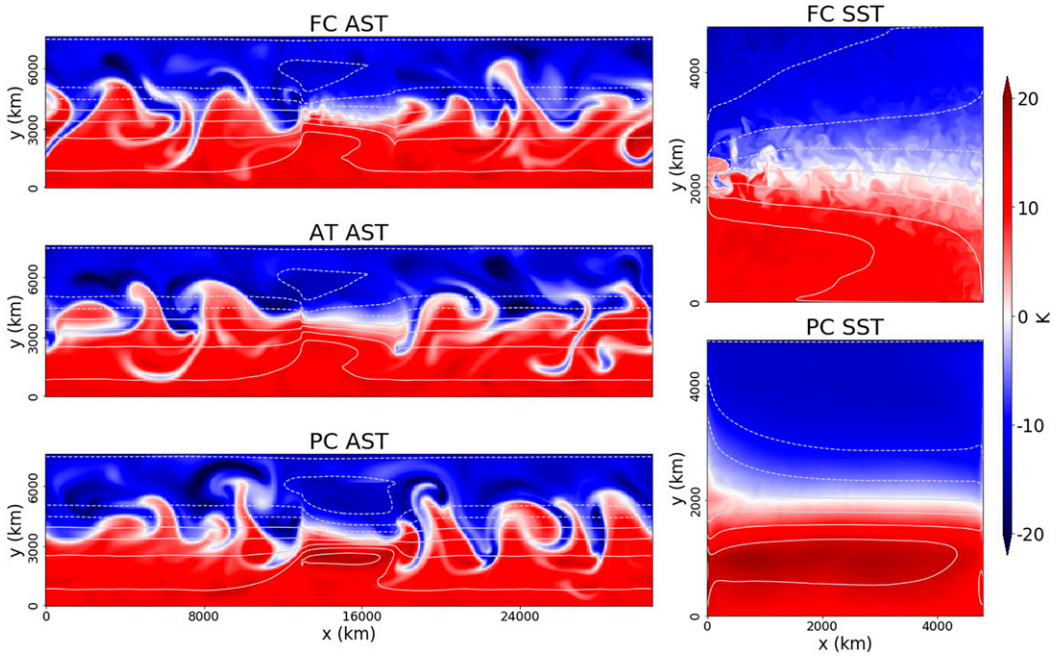

FIG. 2. Atmosphere surface temperature (AST) and sea surface temperature (SST) anomaly snapshots (shaded colors) and 50-yr averages (contours) for the atmosphere and ocean in each model configuration: fully coupled (FC), atmosphere-only (AT), and partially coupled (PC). The static SST field used in the AT configuration is the 50-yr average (depicted by the contours) of FC SST. Contour intervals are 4 K.

(or upper) layer pressure (denoted ${}^{o}p_1$) gradient term (the geostrophic flow that occurs in the model's interior layers) and the ageostrophic Ekman transport contribution:

$$ {}^{o}u_m = -\frac{1}{f_0}{}^{o}p_{1y} + \frac{1}{f_0\,{}^{o}H_m}{}^{o}\tau^{y}, {}^{o}v_m = \frac{1}{f_0}{}^{o}p_{1x} - \frac{1}{f_0\,{}^{o}H_m}{}^{o}\tau^{x}, \quad (3) $$

where τ^x and τ^y are the zonal and meridional components of wind stress, respectively. In PC, the ocean mixed layer velocities are calculated only from the Ekman term, with no contribution from the geostrophic term:

$$ {}^{o}u_m = \frac{1}{f_0\,{}^{o}H_m}{}^{o}\tau^{y}, {}^{o}v_m = -\frac{1}{f_0\,{}^{o}H_m}{}^{o}\tau^{x}. \quad (4) $$

Based on Eq. (4), the ocean's geostrophic circulation in PC is not directly felt by the ocean mixed layer, and therefore neither is it directly felt by the atmosphere. However, we note that the stress is defined by a difference of first layer velocities between the atmosphere and ocean (see formulation in the appendix). We calculate that the ocean dynamics alter the stress by roughly 15%, a small enough margin that we do not consider eddies to be a sizeable contribution to advection in the PC configuration. Without the direct effect of ocean eddies, the SST gradient in the PC case is steeper and thus results in an overestimation of the Ekman dynamics when compared with the FC case.

The difference between FC and PC is visually apparent in Fig. 2, which shows the snapshots (color shading) and 50-yr averages (contours) of surface temperature in each model configuration. There are two noticeable differences between the FC and PC ocean snapshots. First, the eddy field visible in the FC snapshot in Fig. 2 disappears in the PC snapshot due to the near removal of the geostrophic (eddy) advection of temperature in the latter case. Second, the meridional temperature gradient, indicated by the density of contours, is noticeably greater in PC than in FC due to the lack of eddy meridional heat transport. The strong sea surface temperature (SST) gradient is also apparent in the atmosphere surface temperature (AST) field in the PC case, and will play a role in the results discussed below.

The AT model configuration consists of the atmosphere without any dynamic ocean; the ocean is instead represented by a climatologically averaged SST field taken from a 50-yr average of the FC case (shown in Fig. 2 by the contours in the FC SST plot). As depicted in the AT surface temperature plot in Fig. 2, the AT atmosphere's meridional temperature gradient resembles that of FC, but no ocean–atmosphere feedbacks are permitted in this case.

By design, these configurations significantly alter the coupling between ocean and atmosphere, and thus the thermodynamics at the interface between fluids. However, the overall model dynamics are not modified greatly. Comparing the layer kinetic and potential energy in both fluids across model configurations, we find that (over a 10-yr period in each model run) the energetics differ by less than 8%. This similarity in total energetics indicates that the FC, PC, and AT model runs are not entirely dissimilar,

despite many of the differences we note in the air–sea interactions in this manuscript. Through comparison of results from the temperature variance budgets (explained in the next section) across the three model configurations, we aim to diagnose the influence that a dynamic ocean has on the atmosphere, and the importance of both ocean geostrophy and Ekman advection on the surface temperature fields of both fluids.

3. Temperature variance budgets in the frequency domain

The frequency-domain temperature variance budget technique reveals the terms that drive or dampen temperature variance and the time scales at which these terms act. This method is the same as used by Hochet et al. (2020), but we apply it to the surface temperature fields. Our goal is to study air–sea interaction, rather than the deep interior modes of variability focused on in Hochet et al. (2020). Temperature variance (or the square of temperature) is a conserved quantity in Q-GCM. To obtain the temperature variance budget equations in both the ocean and atmosphere, the temperature evolution equations given in Eqs. (1) and (2) are multiplied by twice the corresponding fluid's mixed layer temperature T_m. This yields equations of the form $2T_m(\partial/\partial t)(T_m)$, which is equal to $(\partial/\partial t)(T_m^2)$ (i.e., the time evolution of surface temperature variance). Motivated by our interest in the time scales of model variability, we convert our budget equations into the frequency domain. That is, we take the Fourier transform of each term in the temperature evolution equations [Eqs. (1) and (2)] before multiplying through by twice the Fourier transform of the temperature. Upon integration over the entire x–y domain, we obtain balanced budgets as long as the spun-up model is averaged over a long enough time to neglect the tendency terms. The ocean spectral temperature variance budget is thus

$$0 = 2\iint \left\{ \begin{array}{l} \underbrace{-\mathrm{Re}[{}^{o}\widehat{T_m}^{*}(\widehat{{}^{o}u_m\,{}^{o}T_m})_x] - \mathrm{Re}[{}^{o}\widehat{T_m}^{*}(\widehat{{}^{o}v_m\,{}^{o}T_m})_y]}_{\text{horizontal temperature advection}} + \underbrace{\frac{1}{{}^{o}H_m}\mathrm{Re}[{}^{o}\widehat{T_m}^{*}\widehat{{}^{o}w_{\mathrm{ek}}\,{}^{o}T_m}]}_{\text{vertical temperature advection}} \\ + \underbrace{\frac{1}{{}^{o}\rho^{o}C_p\,{}^{o}H_m}\mathrm{Re}[{}^{o}\widehat{T_m}^{*}\widehat{F_m^{e+}}]}_{\text{entrainment heat flux}} - \underbrace{\frac{1}{{}^{o}\rho^{o}C_p\,{}^{o}H_m}\mathrm{Re}[{}^{o}\widehat{T_m}^{*}\widehat{F_\lambda}]}_{\text{sensible and latent heat flux}} - \underbrace{\frac{1}{{}^{o}\rho^{o}C_p\,{}^{o}H_m}\mathrm{Re}[{}^{o}\widehat{T_m}^{*}(\widehat{F_0^{\uparrow}+F_m^{\downarrow}})]}_{\text{radiative heat flux}} \\ \underbrace{+{}^{o}K_2\mathrm{Re}[{}^{o}\widehat{T_m}^{*}\widehat{\nabla_H^2\,{}^{o}T_m}] - {}^{o}K_4\mathrm{Re}[{}^{o}\widehat{T_m}^{*}\widehat{\nabla_H^4\,{}^{o}T_m}]}_{\text{diffusion}} \end{array} \right\} dx\,dy, \tag{5}$$

where an asterisk (*) represents the complex conjugate and a caret or hat ($\widehat{\cdots}$) denotes a Fourier transform. Note that the solar radiation term integrates to zero over the ocean domain, and hence it does not appear in the above equation.

In the atmosphere, we consider only the portion of the atmosphere that lies directly above the ocean and ignore the regions that are over land. There are two reasons for this choice. First, the Q-GCM atmosphere spans the circumference of the Earth at the relevant latitudes, but the Pacific Ocean equivalent does not exist as we only model one ocean basin (of a size similar to the North Atlantic Ocean). This means that the ratio of land to ocean is unrealistically large in Q-GCM. Second, air–sea coupling is only relevant for the portion of the atmosphere that overlies the ocean. Therefore, the atmosphere temperature variance terms given below are only integrated over the region directly above the ocean. Hence, the solar radiation heat flux from land seen in Eq. (1) is no longer relevant and we do not necessarily expect the terms to balance precisely (as variance is allowed to flux in and out of the ocean region in the atmosphere). The atmosphere temperature variance terms are then as follows:

$$2\iint \left\{ \begin{array}{l} \underbrace{-\mathrm{Re}[{}^{a}\widehat{T_m}^{*}(\widehat{{}^{a}u_m\,{}^{a}T_m})_x] - \mathrm{Re}[{}^{a}\widehat{T_m}^{*}(\widehat{{}^{a}v_m\,{}^{a}T_m})_y]}_{\text{horizontal temperature advection}} - \underbrace{\frac{1}{{}^{a}H^{m}}\mathrm{Re}[{}^{a}\widehat{T_m}^{*}(\widehat{{}^{a}w_{ek}\,{}^{a}T_m})]}_{\text{vertical temperature advection}} \\ \underbrace{-\frac{1}{{}^{a}\rho^{a}C_p}\mathrm{Re}\left[{}^{a}\widehat{T_m}^{*}\frac{\widehat{F_m}}{{}^{a}h_m}\right]}_{\text{heat flux to/from 1st layer}} + \underbrace{\frac{1}{{}^{a}\rho^{a}C_p}\mathrm{Re}\left[{}^{a}\widehat{T_m}^{*}\frac{\widehat{F_\lambda}}{{}^{a}h_m}\right]}_{\text{sensible and latent heat flux}} + \underbrace{\frac{1}{{}^{a}\rho^{a}C_p}\mathrm{Re}\left[{}^{a}\widehat{T_m}^{*}\frac{\widehat{F_m^{\downarrow}+F_0^{\uparrow}}}{{}^{a}h_m}\right]}_{\text{radiative heat flux}} \\ \underbrace{+{}^{a}K_2\mathrm{Re}[{}^{a}\widehat{T_m}^{*}\widehat{\nabla_H^2\,{}^{a}T_m}] - {}^{a}K_4\mathrm{Re}[{}^{a}\widehat{T_m}^{*}\widehat{\nabla_H^4\,{}^{a}T_m}]}_{\text{diffusion}} \end{array} \right\} dx\,dy. \tag{6}$$

The corresponding equations for the full atmospheric domain (not shown) were derived and the budgets were found to balance, as expected over the full domain.

All three model configurations were run for 400 model years after equilibration. Results shown represent averages of seven 100-yr windows, overlapping by 50 years. Before Fourier

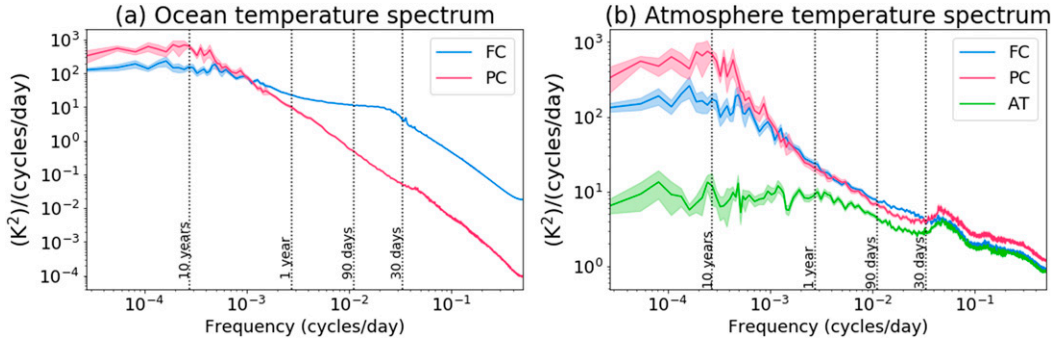

FIG. 3. Temperature spectra in the (a) ocean and (b) atmosphere for all three model configurations: fully coupled (FC), partially coupled (PC), and atmosphere-only (AT). Solid curves are the averages over seven 100-yr time periods and semitransparent shading indicates the 90% confidence interval.

transforms are applied, the mean and trend from the data are removed, and the data are multiplied by a Tukey window (20% taper) function to account for nonperiodicity. Spectral smoothing is applied to the spatially integrated variance terms in this paper, where the amount of smoothing increases with higher frequency. Additionally, 90% confidence intervals of the averaged spectral terms, based on the standard deviation across the seven 100-yr periods, are computed and shown. When we compare magnitudes across different figures, we have calculated the statistical F test to verify that our claims are significant at the 90% level.

Equations (5) and (6) are functions of only frequency ω, after spatial integration. We also show spatial maps of results calculated using the same equations above but without spatial integration, for which each term is instead averaged over frequency bands. Each term in Eqs. (5) and (6) is the product of the Fourier transform of surface temperature with the Fourier transform of the temperature evolution term, and their interpretation thus follows: if the term is positive, it is considered to be driving (or generating) variance in the temperature field. Conversely, a negative term damps temperature variance. Furthermore, the greater the magnitude of a term, the bigger role that term plays in driving (or damping) the variance.

4. Results

a. Temperature spectra

We start by discussing the surface temperature variance frequency spectral density (subsequently referred to simply as "temperature spectra") displayed in Fig. 3. According to the well-known theory of Hasselmann (1976), the ocean responds to atmospheric input of high-frequency variance by integrating this forcing into low-frequency ocean variability. Consequently there is a "reddening" (or steepening) of the ocean temperature spectrum. In Fig. 3a we do indeed see a red spectrum of ocean SST variance. At time scales shorter than about 2 years, the partially coupled (PC) simulation has a steeper slope and lower variance than the fully coupled (FC) model run, affirming that the ocean geostrophic eddy field enhances the high-frequency variability in the ocean. At low frequencies, however, PC has more variability than FC. We will investigate the greater low-frequency variance in PC in the next section.

The atmosphere surface temperature spectra are shown in Fig. 3b. Spectra at high frequencies (corresponding to periods of about 20 days and shorter) are nearly identical (i.e., are not statistically different according to the F test) in the FC and atmosphere-only (AT) simulations, indicating that the choice of a static or dynamic SST field has little effect on the atmosphere at these time scales in this model. However, at the longest time scales (especially beyond 1 year), ocean dynamics have a strong impact on the atmosphere's low-frequency variability, as evidenced by the lower variance in AT than in either FC or PC. While the FC and PC spectra display similarly shaped curves, there are clear differences in the magnitudes of the curves over certain time ranges. At high frequencies, PC shows greater variance through about 30 days than is seen in FC; we posit that this is due to the enhanced background SST gradient in PC compared to FC and will verify this claim in later sections. At slightly longer time scales, from about 30–90 days, FC has greater variance than PC. Because this time span coincides with ocean eddy growth time scales, it is likely that the eddies being generated in the ocean are injecting variance directly into the atmosphere. This assertion will be explored further in section 5. At the lowest frequencies, the fact that both the atmosphere and ocean exhibit greater temperature variance in PC compared to FC hints at the existence of a feedback between the fluids at long time scales. Verifying these claims and determining the processes responsible for this low-frequency coupling are the main goals of this paper.

b. Temperature variance budget in the ocean

In this section, we examine the domain-integrated ocean temperature variance budget terms in frequency space (described in section 3) in both FC and PC model configurations, as shown in Figs. 4a and 4b, respectively. Focusing first on the ocean FC case (Fig. 4a), horizontal advection is seen to be positive and thus drives variance at all frequencies. In fact, it is the only significant driver of variance at time scales shorter than two years. The positive contribution of horizontal advection over all frequencies contrasts with the shift between positive and negative contributions seen by Hochet et al.

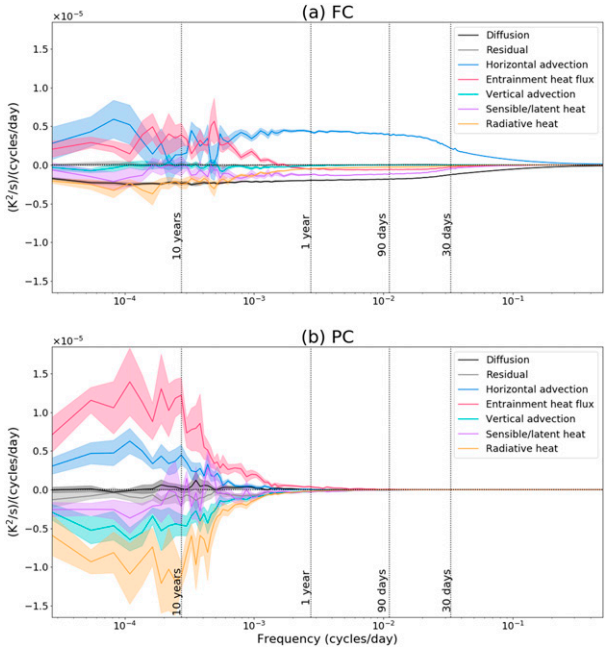

FIG. 4. Frequency-domain ocean temperature variance budgets in the (a) fully coupled (FC) ocean and (b) partially coupled (PC) ocean model configurations. Solid curves are averages over seven 100-yr periods and semitransparent shading indicates the 90% confidence interval.

(2020)—again, their work looks at depth-averaged contributions, which are dominated by geostrophic dynamics and thus exhibit a forward cascade of temperature variance. Near the 2-yr mark, the entrainment heat flux in Fig. 4a switches from removing to adding variance, and at time scales longer than 5 years the entrainment heat flux is of comparable magnitude to the horizontal advection term. Because the entrainment heat flux depends directly on Ekman pumping, the change in sign and the large low-frequency magnitude of the entrainment heat flux indicates an essential role that Ekman pumping plays in driving ocean temperature variance. The remaining terms, namely, the sensible/latent heat and radiative heat flux terms, as well as the diffusion and vertical advection terms, remove variance at nearly all frequencies. The small values of the residual verify that the temperature variance budget is balanced.

The temperature variance terms for PC (Fig. 4b) differ noticeably in shape from those of FC (Fig. 4a) at high frequencies. There is no significant contribution to variance from any PC term at time scales shorter than around 2 years, in contrast to the horizontal advection-driven high frequencies in FC. Because the horizontal advection in PC is Ekman-driven (with only a small geostrophic eddy contribution via wind stress), it appears that Ekman advection does not contribute to the high-frequency variance in the ocean. The dominant driving role of horizontal advection in FC at time scales shorter than 2 years is thus likely due solely to ocean geostrophic eddies. At longer time scales, most terms, notably the entrainment heat flux, display a greater magnitude at low frequencies (time scales longer than around 6 years) in PC relative to FC (verified by an *F* test), consistent with the behavior shown at low frequencies in the ocean spectra depicted in Fig. 3a. The low-frequency horizontal advection terms, however, have similar magnitudes in both FC and PC. With this similarity in magnitude, it would appear that the horizontal advection in FC is mostly driven by Ekman contributions at the longest time scales. However, examination of the spatial maps of temperature variance (Fig. 5, discussed below) demonstrates that ocean geostrophic eddies also play a large role in driving variance at low frequencies. We also note that the diffusion term is not statistically different from zero in the PC run. We attribute the small diffusion to the lack of small-scale dynamics, such as eddies, that do not need to be compensated for in PC.

The variance maps for ocean horizontal advection in FC and PC are shown (color shading) in Fig. 5 with SST contours overlaid. These maps are produced by averaging over frequency bands instead of integrating over the ocean's spatial domain, and reveal the spatial patterns of the temperature variance budget terms across different time ranges. Comparison of the leftmost and rightmost columns in Fig. 5, depicting horizontal advection in FC and PC respectively, demonstrates that the spatial patterns differ significantly, with the PC pattern aligning with the ocean gyres and FC dominated by the western boundary current separation (CS) region.

We can understand the FC pattern better by separating the contributions from geostrophic and Ekman flow components (respectively displayed in the middle-left and middle-right columns in Fig. 5). This separation of contributions to horizontal advection allows us to compare the Ekman contribution to advection within the FC run (with ocean eddies present) with that of the PC run where horizontal advection depends only on Ekman transport. Comparing these two Ekman-only advection terms (the two rightmost columns in Fig. 5), similar spatial patterns emerge in the lowest frequency band (2–100 years), but the magnitude of this pattern in the PC domain is significantly greater than in the FC domain. Based on the displayed coalignment with the SST contours, the greater magnitude in PC is likely due to the larger meridional SST gradient in PC than in FC. Contours of mixed layer velocities in FC and PC were also plotted and do not align with the Ekman advection spatial patterns, thus supporting our claim that the SST gradient is the primary mechanism responsible for the large Ekman advection magnitude in the PC run. At higher frequencies, Ekman transport has a negligible contribution to both FC and PC temperature variance. A slight exception is the weak signal from FC Ekman transport in the CS region in the middle frequency band; this weak signal is not visible in the PC simulation. Despite the smaller magnitudes, the weak Ekman signal in the CS region indicates that the Ekman and geostrophic eddy fields interact in the FC regime—a type of communication severely reduced in the PC run. We also note the extent of cancellation in the domain-integrated terms, particularly in the low-frequency maps of Ekman-driven advection.

Comparing across the middle two columns of Fig. 5, it is clear that the ocean eddy-driven CS region generates variance at all frequencies, and dominates the variance in the higher two frequency bands shown. The ocean eddy field, therefore, is the

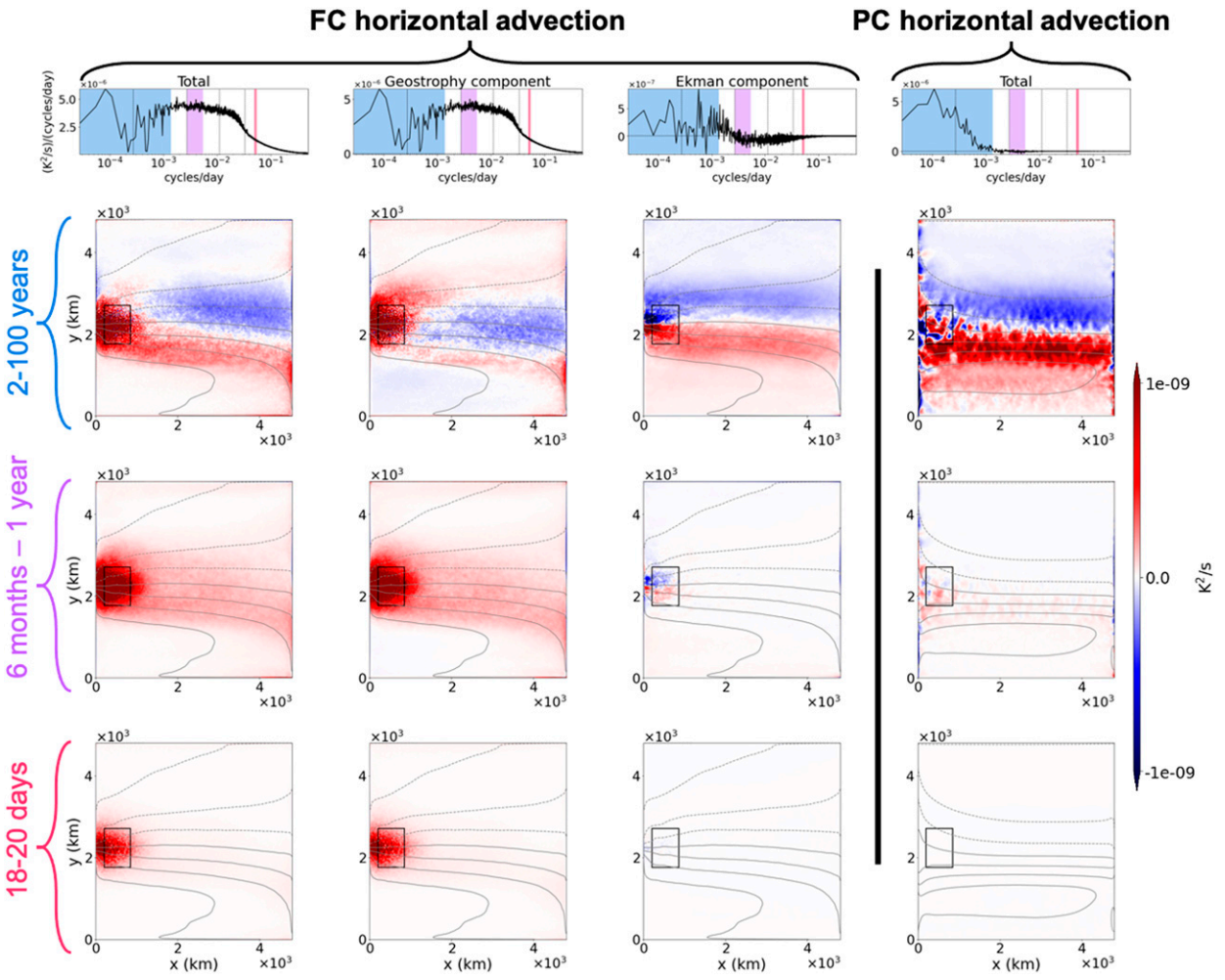

FIG. 5. Spatial maps of the ocean fully coupled (FC) and partially coupled (PC) horizontal advection temperature variance budget terms. (top) The domain-integrated term as a function of frequency. (remaining rows) Maps of frequency band-averaged budget terms: 2 to 100 years (highlighted in blue in the domain-integrated term shown in the top row), 6 months to 1 year (highlighted in purple), and 18 to 20 days (highlighted in pink). (left),(right) The full horizontal advection term for FC and PC, respectively. (center left) The geostrophic eddy component and (center right) the horizontal Ekman component of horizontal advection in the FC case. Contours of SST averaged over 50 years are shown in gray with intervals of 4 K. The rectangle outlined in black is the western boundary current separation (CS) region.

principal driver of horizontal advection and thus variance at annual and shorter time scales. Only in the lowest frequency band is there a substantial input from Ekman processes. Outside the CS region, the geostrophic and Ekman components of low-frequency FC horizontal advection show similar magnitudes, yielding the combined asymmetric pattern shown in the total FC horizontal advection term. Thus, Ekman and geostrophic eddy flows are of similar importance in their contributions to low-frequency temperature variance outside of the CS region. Still, the largest magnitudes of variance input due to horizontal advection stem from the eddies in the CS region, even at the lowest frequencies. The variance maps show that while Ekman advection takes on its largest values at low frequencies (as observed in the domain-integrated PC plot in the top row of Fig. 5), the geostrophic eddy-driven CS region drives variance at all frequency bands, including the lowest. This observation contradicts the claim suggested earlier that Ekman advection is the primary contributor to low-frequency variance input of the FC horizontal advection.

In the domain-integrated ocean budget (Fig. 4a), the entrainment heat flux (which depends directly on both Ekman pumping and the temperature difference between ocean mixed-layer and upper-layer temperature) adds variance at low frequencies in FC and even more so in PC, and displays interesting behavior shifting from negative to positive contributions in FC. Motivated by the change in sign, we examine spatial maps of the entrainment heat flux contribution to the temperature variance budget (Fig. 6). Maps for two different time ranges are shown: from 2 to 100 years (highlighting the positive values of the entrainment heat flux term) and from

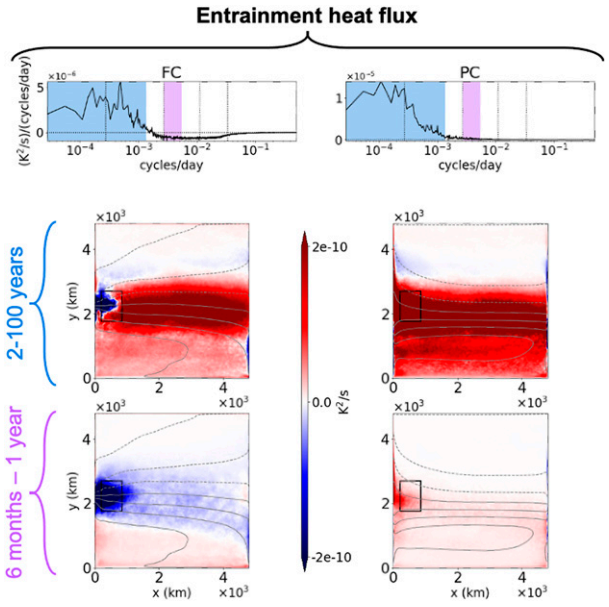

FIG. 6. Spatial maps of the ocean entrainment heat flux temperature variance term in the (left) fully coupled (FC) and (right) partially coupled (PC) configurations. (top) The domain-integrated term as a function of frequency. (middle),(bottom) Maps of frequency band-averaged budget terms for (middle) 2 to 100 years (highlighted in blue in the top row) and (bottom) 6 months to 1 year (highlighted in purple in the top row). Contours of SST averaged over 50 years are shown in gray with intervals of 4 K. The rectangle outlined in black is the western boundary current separation (CS) region.

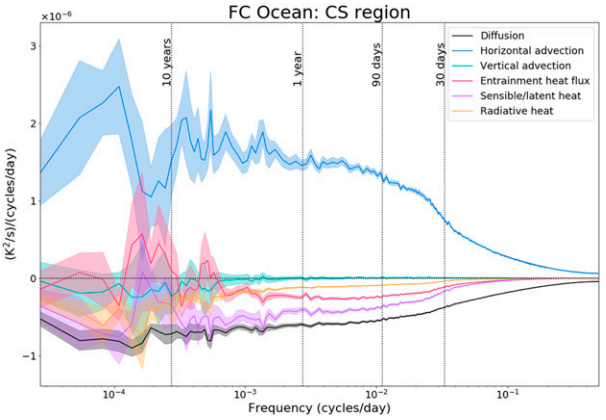

FIG. 7. Frequency-domain temperature variance budget in the fully coupled (FC) ocean's western boundary current separation (CS) region, depicted by the black-outlined rectangle in Figs. 5 and 6. Solid curves are averages over seven 100-yr periods and semi-transparent shading indicates the 90% confidence interval.

6 months to 1 year (highlighting the negative values in FC). The CS region shows a distinctive signature in FC that is not present in PC. Across both frequency bands, the CS region in FC acts to dampen the variance due to entrainment contributions. However, the different patterns between the two frequency bands in FC indicate the source of the sign change in the domain-integrated term: the region where the two gyres meet, between the CS region and the eastern ocean boundary. This positive region in the FC 2–100-yr results coincides with the atmospheric storm track and we infer that the large input of temperature variance due to the entrainment heat flux stems from atmospherically driven mechanisms, partially driven by Ekman pumping. The negative eddy signature in the CS region opposes the large variance input by entrainment along the gyre boundaries in FC and is essentially nonexistent in PC–another indication that the ocean geostrophic eddy field completely dominates the CS region, and also that this region has different dynamics than the rest of the domain. Overall, the entrainment heat flux spatial signature suggests that low-frequency (time scales longer than 2 years) ocean temperature variability is largely driven by coupling with the atmosphere, particularly outside of the CS region.

The above results make it clear that the CS region plays a crucial role in variance behavior, in that it shows a distinctly different pattern and greater magnitude of variance than the rest of the ocean domain, in line with results from Martin et al. (2020) that showed the CS region is important for the nonlinear advection of kinetic energy. To further examine the behavior in the CS region of the FC ocean, we have plotted the CS spatially integrated SST variance terms in Fig. 7. As was apparent from the spatial maps in Fig. 5, horizontal advection adds to the variance; in fact we can now see that it is essentially the only term that adds variance in the CS region. Separation of the geostrophic and Ekman components of horizontal advection (Fig. 5) demonstrates that the majority of the variance-generating behavior in the CS horizontal advection term is due to the direct influence of ocean geostrophic eddies on advection. All other terms dampen the variance at all frequencies.

c. *Temperature variance budget in the atmosphere*

We now turn our attention to the atmosphere temperature variance budget, and we remind the reader that we are only considering the portion of the atmosphere that lies directly above the ocean. In Fig. 8 we compare three different model configurations—FC, PC, and AT (atmosphere-only)—all plotted with the same *y*-axis scaling for ease of comparison. As in the ocean, horizontal advection plays a dominant role particularly at time scales shorter than annual in all three model runs. The shapes and magnitudes of the curves are similar across model configurations at time scales shorter than about 2 years. At periods greater than 2 years, radiative heat flux is the dominant driver of variance in both PC and FC. However, the magnitude of radiative heat flux in PC is roughly 3 times larger than that of FC. Radiative heat depends on both ocean and atmosphere surface temperature and, based on comparison with the AT results, where it is close to zero across all frequencies, it is clearly influenced by the presence of ocean dynamics. Thus, the low-frequency atmosphere is also driven by a process that stems from coupling with the ocean, further verifying the existence of a low-frequency feedback between ocean and atmosphere.

As in the ocean, insight into the behavior of specific atmospheric terms can be obtained from spatial maps. Maps of the

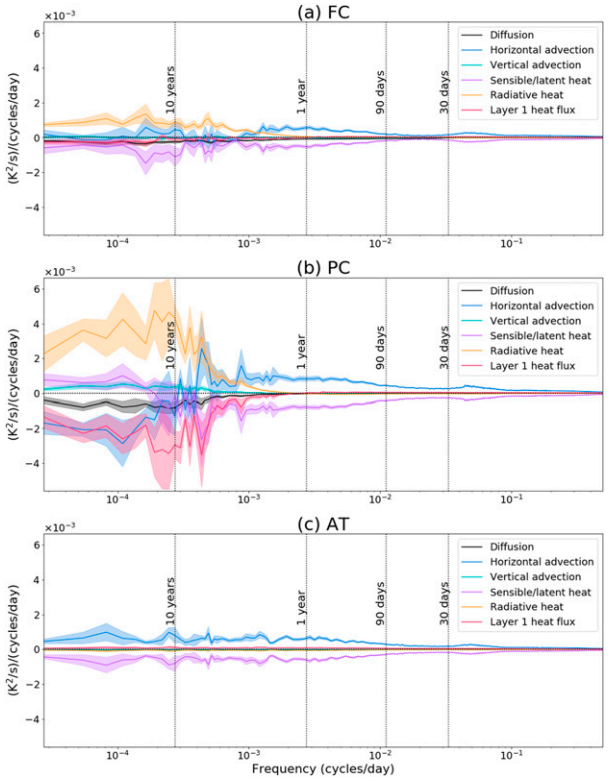

FIG. 8. Frequency-domain temperature variance budgets in the atmosphere (lying just above the ocean) in the (a) fully coupled (FC), (b) partially coupled (PC), and (c) atmosphere-only (AT) model configurations. Solid curves are averages over seven 100-yr periods and semitransparent shading indicates the 90% confidence interval.

atmosphere's horizontal advection (left three columns) and radiative heat flux (right three columns) contributions to the temperature variance budget for each of the three model configurations (columns), and across three frequency bands (rows) of 2 to 100 years, 6 months to 1 year, and 18 to 20 days, are presented in Fig. 9. As in Fig. 5, temperature, in this case the time-averaged atmosphere surface temperature (AST), is contoured. In the highest frequency band shown, the spatial pattern and sign of horizontal advection is similar across all three model runs, but the PC map shows a greater magnitude over the eastern storm track region, aligned with the steepest gradient of AST. This increased magnitude in PC compared with FC and AT is thus likely due to the increased meridional SST gradient in PC, and is also the apparent source of the increased high-frequency variance in the PC AST spectrum in Fig. 3b. In the midfrequency band shown in Fig. 9, both FC terms display distinctly different behavior in the CS region (the region that lies directly above the ocean's CS region) than in either PC or AT, and this CS pattern persists at the lowest frequency band, but not in the highest band. We thus find that the ocean geostrophic eddy field has an effect on the atmosphere, but predominantly in the CS region and at the lower frequencies. The transition frequency (at which the impact of ocean eddies is visible in the atmospheric domain) is discussed in section 5.

The lowest frequency band displayed in Fig. 9 shows distinctive behavior compared with the other frequency bands. For both horizontal advection and radiative heat, the spatial pattern in FC and PC are similar and differ significantly from that in AT. The greater magnitude of the values in PC compared with FC is again attributed to the steeper temperature gradient in PC. The similarity in spatial pattern between FC and PC suggests that the spatial pattern of temperature variance in the low-frequency atmosphere is set up by the ocean's Ekman advection, which is nonexistent in AT. In addition, the effect of the Ekman term is exaggerated in PC compared to FC due to the larger temperature gradient, and so we would expect any behavior due to Ekman advection to display greater magnitude in PC than in FC. The connection between radiative heat and Ekman processes is of particular importance since Figs. 8a and 8b show that radiative heat flux is the primary driver of low-frequency variance in the atmosphere. We therefore assert that the low-frequency feedback from the ocean to the atmosphere occurs via radiative heat, but underlying this process is forcing from the Ekman transport in the ocean. The other difference between the FC and PC patterns in both terms is the larger magnitude over the CS region compared with the rest of the domain in FC. As discussed previously, the larger FC CS magnitudes are attributed to ocean geostrophic eddies.

5. Discussion and conclusions

We have used a new surface temperature variance budget frequency technique to identify the underlying drivers of surface temperature variability in the ocean and atmosphere across a wide range of time scales in the medium-complexity Quasi-Geostrophic Coupled Model. We build upon Hasselmann's (1976) result that the ocean integrates high-frequency atmospheric forcing into low-frequency variability. Our main findings can be summed up as follows:

- Horizontal advection is essentially the only driver of variance in each fluid (the ocean and the atmosphere) at annual and shorter time scales. In the ocean, subannual horizontal advection is found to be almost entirely driven by geostrophic eddies.
- From interannual to multidecadal time scales, the main driving terms of surface temperature variance in both the ocean and atmosphere are due to coupling between the two fluids. Through decomposition of the temperature variance budget and comparison across model configurations, we have determined that Ekman processes are at the core of the low-frequency coupling between the ocean and atmosphere in Q-GCM. Specifically, the ocean surface temperature variability is largely driven by Ekman pumping via the entrainment heat flux [especially outside of the western boundary current separation (CS) region], while the atmosphere surface temperature variability is mostly driven by radiative heat transfer from the ocean, that is itself largely determined by the Ekman transport contribution to horizontal ocean advection.

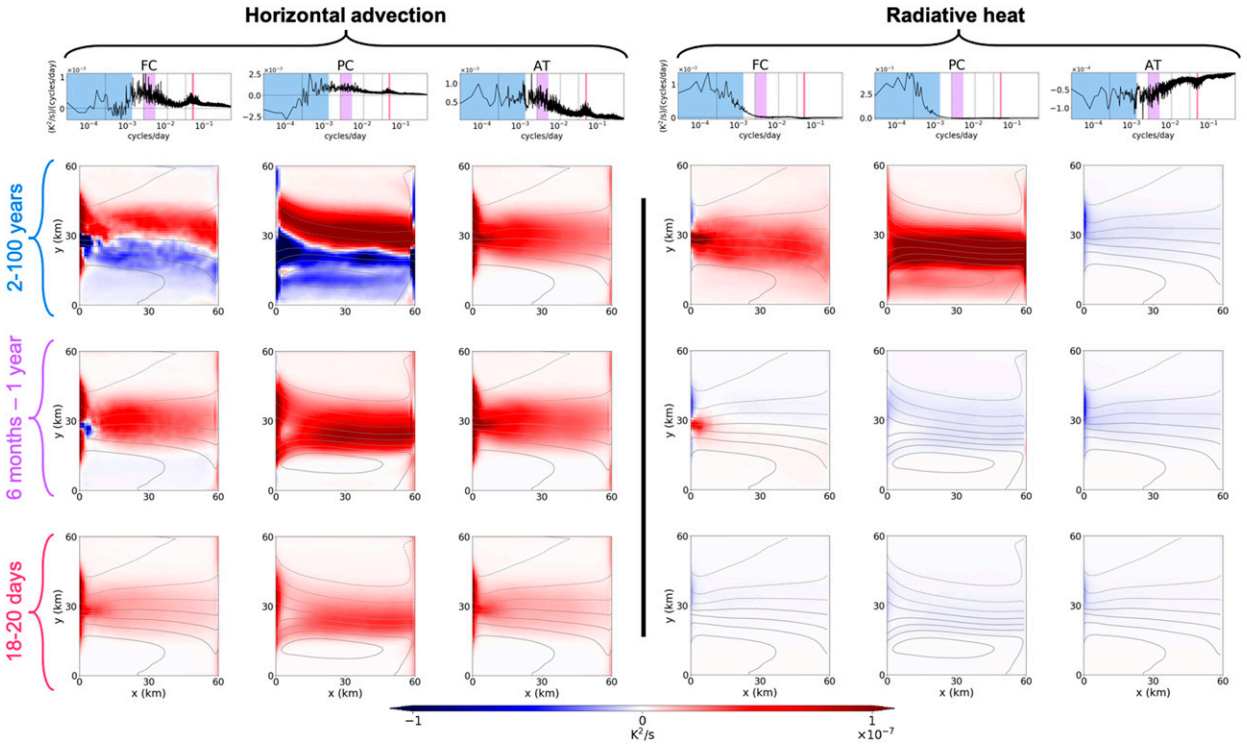

FIG. 9. Spatial maps of the (left three columns) atmospheric horizontal advection and (right three columns) radiative heat temperature variance budget terms over the ocean. Three model configurations are shown: fully coupled (FC), partially coupled (PC), and atmosphere-only (AT). (top) The spatially integrated term as a function of frequency. (remaining rows) Maps of frequency band-averaged budget terms for the low-frequency band (2 to 100 years, highlighted in blue in the top row), the middle-frequency band (6 months to 1 year, highlighted in purple), and the high-frequency band (18 to 20 days, highlighted in pink). Contours of atmosphere surface temperature averaged over 50 years are shown in gray with intervals of 4 K.

- Ocean geostrophic eddies drive ocean variance at all time scales in this study, and are imprinted onto the atmosphere in the CS region at long time scales.

The influence of ocean geostrophic eddies on surface temperature variance is made clear in our analysis through comparison of the fully coupled (FC) system with the partially coupled (PC) system, where in the latter ocean horizontal advection depends on Ekman transport processes only (noting that there is a weak dependence on geostrophy due to the relative wind stress). In the ocean, horizontal advection is driven by ocean eddies at time scales shorter than annual. At longer time scales, eddies continue to play a role, particularly in the CS region, but are of similar magnitude as the Ekman contribution to horizontal advection outside of the CS region. Hence, the ocean geostrophic eddy field plays a major role throughout the ocean domain, but particularly at high frequencies and in the CS region.

Our ocean CS results agree with and extend the western boundary current region results from recent studies by Buckley et al. (2015) and Small et al. (2020). They both find that geostrophic contributions to advection drive ocean surface temperature variance, while surface heat fluxes (sensible/latent heat flux + radiative heat flux) dampen variance in the western boundary current region, as we also observe (Fig. 7). However, in their frequency-domain analysis, Buckley et al. (2015) find that ocean dynamics do not play a role until interannual and longer time scales. Using a higher-resolution model that resolves eddies, Small et al. (2020) find that this balance of advection and air–sea fluxes in the western boundary current region holds true at least at monthly time scales, contradicting the claim of Buckley et al. (2015) that ocean dynamics are only important at interannual and longer time scales. Our study combines the use of a frequency-domain analysis with an eddy-resolving, multidecadal ocean model to show that horizontal advection drives variance in the ocean CS region at all time scales resolved in this study, from multidecadal down to nearly daily time scales.

In contrast to Buckley et al. (2015), Small et al. (2020) also observe that ocean advection adds variance in regions outside of the CS area. While the largest values of variance input in the Q-GCM ocean from horizontal advection stem from the CS region, Fig. 5 reveals that horizontal advection drives variance throughout the ocean. At subannual time scales, the geostrophic eddy contribution to advection adds variance along the atmospheric storm track and at longer time scales

Ekman advection adds variance in the subtropical gyre. The Ekman and geostrophic components of advection are also distinguished in Small et al. (2020), and geostrophic eddies are found to dominate the advection term, consistent with the results presented here, particularly at the monthly time scales investigated by Small et al. (2020). Through examination of lower-frequency behavior than was studied in Small et al. (2020), we have further shown that at interannual and longer time scales the Ekman and geostrophic components contribute similarly (in magnitude) to advection outside of the CS region, but with differing spatial patterns (shown in the middle two columns of Fig. 5).

We have found that Ekman processes play a major role in driving variability at low frequencies in both fluids, particularly outside of the CS region. The dominance of Ekman heat transport has also been noted by Larson et al. (2018), who find that SST variance is noticeably reduced in the midlatitudes in the absence of Ekman processes, particularly at the decadal time scale (this time scale was especially apparent over the North Pacific Ocean). Our results are in agreement that Ekman advection plays a major role driving SST variance at long time scales, although, by resolving eddies in our model, we determine that ocean eddies are also a large contributor to low-frequency variance. Additionally, while we do not investigate the effect of spatial scale on temperature variance, Small et al. (2020) find that Ekman advection acts at large spatial scales, which is in line with findings by both Buckley et al. (2015) and Larson et al. (2018) regarding large Ekman-driven variability in their low-resolution (i.e., not eddy-resolving) models. With our result that Ekman advection acts at low frequencies, we suggest that Ekman processes are important for driving oceanic variability at both large spatial scales and long time scales (interannual to multidecadal).

It is well known that the ocean eddy-driven western boundary currents can directly influence the atmosphere, particularly on the location of the storm track via moisture-driven and cloud-feedback processes (e.g., Small et al. 2008; Minobe et al. 2008; Smirnov et al. 2015; Kirtman et al. 2017). Because the Q-GCM atmosphere does not include moisture, it is difficult to compare specific mechanisms between our study and studies employing more realistic models. Our work does show that, even without explicitly resolved moisture processes, the CS region locally impacts the atmosphere surface boundary layer at the longer time scales (visible in both horizontal advection and radiative heat maps shown in Fig. 9). Although not shown in this manuscript, the distinct CS dynamics become visible in the atmosphere at around 30 days in both the horizontal advection and radiative heat terms, with the magnitude increasing with time scale. Thus, ocean eddies are capable of directly affecting the atmosphere, by injecting variance at ocean eddy time scales in addition to a more integrated effect at the longer time scales. This observation also validates the claim made in section 4a that the greater variance in the FC, compared with the PC, atmosphere between 30 and 90 days (Fig. 3b) can be explained by the distinct pattern due to ocean eddies in the CS region. CS-region ocean eddies also impact the atmosphere at time scales longer than 90 days, but their effect is overtaken by other processes elsewhere in the domain.

Many previous studies on the topic of air–sea coupling stress the importance of the surface heat fluxes on ocean temperature variability. For instance, Gulev et al. (2013) calculate the correlation of SST and sensible/latent heat flux in observations, to confirm the claim by Bjerknes (1964) that the atmosphere drives SST variability at short (subdecadal) time scales while the ocean drives SST variability at long (multidecadal) time scales (outside of eddying regions). Their reasoning relies on the assumption that the surface heat fluxes are atmospherically driven such that if there is correlation between sensible/latent heat flux and the SST field, this indicates that the atmosphere is driving SST. Our approach instead suggests that surface heat fluxes tend to dampen the ocean's SST variability more than drive it (see Fig. 4a). Furthermore, we consider the surface heat fluxes to be inherently coupled terms, and have shown that the radiative heat flux in the atmosphere is largely driven by Ekman advection in the ocean, which itself arises from atmospheric winds. Our results show that it is difficult to determine whether the atmosphere drives the ocean or vice versa, but we can conclude that there is intense coupling occurring at interannual and multidecadal time scales generating variability in both the ocean and atmosphere.

Coupled modes of low-frequency variability at near-decadal time scales (on par with the low-frequency ocean–atmosphere coupling we find in this study) have been highlighted in numerous other studies, and have been attributed to various mechanisms such as advection (Sutton and Allen 1997; Menary et al. 2015) or mechanical ocean–atmosphere feedback (Wu and Liu 2005; Kravtsov et al. 2007). Our results point to advection as playing a major role in temperature variance in both fluids, especially in the western boundary current. However, we attribute the low-frequency coupling observed in this study to a combination of Ekman processes and radiative heat flux. While we do not examine specific modes of variability, the mechanisms underlying the low-frequency ocean–atmosphere coupling in this paper could help pinpoint the driving forces of such decadal-scale coupled modes.

This work has been carried out on a dynamically rich but still idealized ocean–atmosphere model, without small-scale processes like atmospheric convective storms or cloud feedbacks, which are known to be important in air–sea interaction (e.g., Small et al. 2008; Minobe et al. 2008). However, our results can guide the analysis of more realistic models in which it may not be feasible to calculate or save all of the terms necessary to close the temperature variance budget. Specifically we have used a novel frequency-domain approach to show that advection and Ekman processes are key players in air–sea coupling, and that interannual to multidecadal climate variability is dominated by coupling between the two fluids. As a complement to the ever increasing resolution and complexity of global climate models, we wish to stress the potential of medium-complexity models such as Q-GCM to enrich our understanding of the physical processes involved in air–sea coupling.

Acknowledgments. The authors wish to thank James Munroe, Jeff Blundell, Andrew Kiss, Aidan Heerdegen, William Dewar, Navid Constantinou, and Bruno Deremble for helpful discussions and model setup. This material is based upon work supported by the National Science Foundation Graduate Research

Fellowship under Grant DGE 1256260. PEM also acknowledges the associated Graduate Research Opportunities Worldwide fellowship to conduct research at the Australian National University. Q-GCM and analysis were run on the National Computational Infrastructure (NCI), which is supported by the Australian Government. The codes are written in Python with the Pangeo environment. Specific software used includes NumPy (Harris et al. 2020), Matplotlib (Hunter 2007), xarray (Hoyer and Hamman 2017), and Dask (Dask Development Team 2016). PEM and BKA acknowledge support from NSF Grants OCE-0960820, OCE-1351837, and OCE-1851164, and the University of Michigan African Studies Center and M-Cubed program, the latter supported by the Office of the Provost and the College of Literature, Science, and the Arts.

Data availability statement. The Quasi-Geostrophic Coupled Model (Q-GCM) is available for free download at www.q-gcm.org. Q-GCM can be identically re-run as in the present work by choosing the North Atlantic configuration with the parameters listed in Tables 1 and A1.

APPENDIX

Heat Flux Formulations in Q-GCM

The heat flux terms in Eqs. (1) and (2) are defined as follows (with the superscript *o* denoting ocean and superscript *a* denoting atmosphere). At the air–sea boundary the heat flux formulations are as follows:

$$\text{Atmosphere:}\begin{cases} F_m^{\downarrow} + F_\lambda + F_0^{\uparrow} \rightarrow \text{Over ocean} \\ F_s \rightarrow \text{Over land} \end{cases}$$

$$\text{Ocean:}\begin{cases} {}^oF_0 = -F_\lambda - F_0^{\uparrow} - F_m^{\downarrow} - F_s, \\ F_\lambda = \lambda({}^oT_m - {}^aT_m) \rightarrow \text{Sensible and latent heat} \\ F_0^{\uparrow} = D_0^{\uparrow}{}^oT_m \rightarrow \text{Oceanic radiative heat} \\ F_m^{\downarrow} = D_m^{\downarrow}{}^aT_m \rightarrow \text{Atmospheric radiative heat over ocean} \end{cases}$$

$$F_s(y) = \frac{F_{s'}}{2}\sin\left[\frac{\pi(y-y_0)}{{}^aY}\right] \rightarrow \text{Incoming shortwave solar radiation.} \tag{A1}$$

At the boundary of the mixed layer with the quasigeostrophic layer 1, the heat flux formulations are the following:

$$\begin{aligned} &\text{Atmosphere:}\{F_m = F_m^{\uparrow} + F_1^{\downarrow} + {}^aF_m^{e-} \\ &F_m^{\uparrow} = B_m^{\uparrow}{}^a\eta_m + D_m^{\uparrow}{}^aT_m \rightarrow \text{Upward atmospheric mixed layer radiation} \\ &F_1^{\downarrow} = A_{1,1}^{\downarrow}{}^a\eta_1 + B_1^{\downarrow}{}^a\eta_m \rightarrow \text{Downward atmospheric layer 1 radiation} \\ &{}^aF_m^{e-} = {}^a\phi_m{}^a\eta_m \rightarrow \text{Atmospheric entrainment heat flux} \\ &\text{Ocean:}\{{}^oF_m^{e+} = -0.5{}^o\rho{}^oC_p({}^oT_m - {}^oT_1)w_{\text{ek}}. \\ &{}^oF_m^{e+} \rightarrow \text{Oceanic entrainment heat flux} \end{aligned} \tag{A2}$$

TABLE A1. Constants in Q-GCM heat flux terms.

Parameter	Value
λ	35
${}^a\phi_m$	0.15
$D_0^{\uparrow}$	6.427
$D_m^{\downarrow}$	−3.234
$B_m^{\uparrow}$	−0.021
$D_m^{\uparrow}$	2.965
$A_{1,1}^{\downarrow}$	$1.686\,32 \times 10^{-3}$
$B_1^{\downarrow}$	0.011

The atmosphere surface perturbation height is denoted ${}^a\eta_m$ and first layer height perturbation ${}^a\eta_1$. The constant ${}^a\phi_m$ is the rate of relaxation of atmospheric mixed layer height anomalies.

As mentioned in section 2a, the atmospheric mixed layer height evolves in time and is given by

$$\frac{\partial}{\partial t}({}^ah_m) = -({}^au_m{}^ah_m)_x - ({}^av_m{}^ah_m)_y - {}^ae_m, \tag{A3}$$

where

$${}^ae_m = \frac{{}^a\phi_m}{{}^a\rho{}^aC_p({}^aT_1 - {}^aT_m)}{}^a\eta_m. \tag{A4}$$

The stress formulation in the atmosphere is given by

$$\begin{cases} {}^a\tau^x = C_D\dfrac{M({}^av_1 - {}^ov_1) + (a+b)M({}^au_1 - {}^ou_1)}{1 + (a+b)^2M^2} \\ {}^a\tau^y = C_D\dfrac{M({}^au_1 - {}^ou_1) - (a+b)M({}^av_1 - {}^ov_1)}{1 + (a+b)^2M^2}, \end{cases} \tag{A5}$$

where

$$M = |{}^a\mathbf{u}_m - {}^o\mathbf{u}_m|, a = \frac{C_D}{{}^aH_mf_0}, b = \frac{{}^a\rho C_D}{{}^o\rho{}^oH_mf_0}. \tag{A6}$$

Many of the variables and constants used above have already been described in section 2 or in Table 1. The values of the remaining parameters shown here are included in Table A1. All nonderived model parameters were tuned by Jeff Blundell and Chris Wilson (personal communication, 19 May 2015), based on the method explained in Wilson et al. (2015) section 2a.

REFERENCES

Arbic, B. K., R. B. Scott, G. R. Flierl, A. J. Morten, J. G. Richman, and J. F. Shriver, 2012: Nonlinear cascades of surface oceanic geostrophic kinetic energy in the frequency domain. *J. Phys. Oceanogr.*, **42**, 1577–1600, https://doi.org/10.1175/JPO-D-11-0151.1.

——, M. Müller, J. G. Richman, J. F. Shriver, A. J. Morten, R. B. Scott, G. Sérazin, and T. Penduff, 2014: Geostrophic turbulence in the frequency–wavenumber domain: Eddy-driven low-frequency variability. *J. Phys. Oceanogr.*, **44**, 2050–2069, https://doi.org/10.1175/JPO-D-13-054.1.

Barsugli, J. J., and D. S. Battisti, 1998: The basic effects of atmosphere–ocean thermal coupling on midlatitude variability. *J. Atmos. Sci.*, **55**, 477–493, https://doi.org/10.1175/1520-0469(1998)055<0477:TBEOAO>2.0.CO;2.

Bishop, S. P., R. J. Small, F. O. Bryan, and R. A. Tomas, 2017: Scale dependence of midlatitude air–sea interaction. *J. Climate*, **30**, 8207–8221, https://doi.org/10.1175/JCLI-D-17-0159.1.

Bjerknes, J., 1964: *Atlantic Air–Sea Interaction*. Advances in Geophysics, Vol. 10, Elsevier, 82 pp., https://doi.org/10.1016/S0065-2687(08)60005-9.

Buckley, M. W., R. M. Ponte, G. Forget, and P. Heimbach, 2014: Low-frequency SST and upper-ocean heat content variability in the North Atlantic. *J. Climate*, **27**, 4996–5018, https://doi.org/10.1175/JCLI-D-13-00316.1.

——, ——, ——, and ——, 2015: Determining the origins of advective heat transport convergence variability in the North Atlantic. *J. Climate*, **28**, 3943–3956, https://doi.org/10.1175/JCLI-D-14-00579.1.

Chelton, D. B., M. G. Schlax, M. H. Freilich, and R. F. Milliff, 2004: Satellite measurements reveal persistent small-scale features in ocean winds. *Science*, **303**, 978–983, https://doi.org/10.1126/science.1091901.

Dask Development Team, 2016: Dask: Library for dynamic task scheduling. https://dask.org.

Deremble, B., G. Lapeyre, and M. Ghil, 2012: Atmospheric dynamics triggered by an oceanic SST front in a moist quasi-geostrophic model. *J. Atmos. Sci.*, **69**, 1617–1632, https://doi.org/10.1175/JAS-D-11-0288.1.

Frankignoul, C., and K. Hasselmann, 1977: Stochastic climate models, Part II: Application to sea-surface temperature anomalies and thermocline variability. *Tellus*, **29**, 289–305, https://doi.org/10.3402/tellusa.v29i4.11362.

Gulev, S. K., M. Latif, N. Keenlyside, W. Park, and K. P. Koltermann, 2013: North Atlantic Ocean control on surface heat flux on multidecadal timescales. *Nature*, **499**, 464–467, https://doi.org/10.1038/nature12268.

Harris, C. R., and Coauthors, 2020: Array programming with NumPy. *Nature*, **585**, 357–362, https://doi.org/10.1038/s41586-020-2649-2.

Hasselmann, K., 1976: Stochastic climate models. Part I: Theory. *Tellus*, **28**, 473–485, https://doi.org/10.3402/tellusa.v28i6.11316.

Hayashi, Y., 1980: Estimation of nonlinear energy transfer spectra by the cross-spectral method. *J. Atmos. Sci.*, **37**, 299–307, https://doi.org/10.1175/1520-0469(1980)037<0299:EONETS>2.0.CO;2.

Hochet, A., T. Huck, O. Arzel, F. Sévellec, A. Colin de Verdière, M. Mazloff, and B. Cornuelle, 2020: Direct temporal cascade of temperature variance in eddy-permitting simulations of multidecadal variability. *J. Climate*, **33**, 9409–9425, https://doi.org/10.1175/JCLI-D-19-0921.1.

Hogg, A. M., W. K. Dewar, P. D. Killworth, and J. R. Blundell, 2003: A quasi-geostrophic coupled model (Q-GCM). *Mon. Wea. Rev.*, **131**, 2261–2278, https://doi.org/10.1175/1520-0493(2003)131<2261:AQCMQ>2.0.CO;2.

——, ——, ——, and ——, 2006: Decadal variability of the midlatitude climate system driven by the ocean circulation. *J. Climate*, **19**, 1149–1166, https://doi.org/10.1175/JCLI3651.1.

——, J. R. Blundell, W. K. Dewar, and P. D. Killworth, 2014: Formulation and users' guide for Q-GCM. https://q-gcm.org/downloads.html.

Hoyer, S., and J. Hamman, 2017: xarray: N-D labeled arrays and datasets in Python. *J. Open Res. Software*, **5**, 10, https://doi.org/10.5334/jors.148.

Hunter, J. D., 2007: Matplotlib: A 2D graphics environment. *Comput. Sci. Eng.*, **9**, 90–95, https://doi.org/10.1109/MCSE.2007.55.

Kirtman, B. P., and Coauthors, 2012: Impact of ocean model resolution on CCSM climate simulations. *Climate Dyn.*, **39**, 1303–1328, https://doi.org/10.1007/s00382-012-1500-3.

——, N. Perlin, and L. Siqueira, 2017: Ocean eddies and climate predictability. *Chaos*, **27**, 126902, https://doi.org/10.1063/1.4990034.

Kravtsov, S., W. Dewar, P. Berloff, J. McWilliams, and M. Ghil, 2007: A highly nonlinear coupled mode of decadal variability in a mid-latitude ocean–atmosphere model. *Dyn. Atmos. Oceans*, **43**, 123–150, https://doi.org/10.1016/j.dynatmoce.2006.08.001.

Kushnir, Y., W. A. Robinson, I. Bladé, N. M. J. Hall, S. Peng, and R. Sutton, 2002: Atmospheric GCM response to extratropical SST anomalies: Synthesis and evaluation. *J. Climate*, **15**, 2233–2256, https://doi.org/10.1175/1520-0442(2002)015<2233:AGRTES>2.0.CO;2.

Lambaerts, J., G. Lapeyre, R. Plougonven, and P. Klein, 2013: Atmospheric response to sea surface temperature mesoscale structures. *J. Geophys. Res. Atmos.*, **118**, 9611–9621, https://doi.org/10.1002/jgrd.50769.

Larson, S. M., D. J. Vimont, A. C. Clement, and B. P. Kirtman, 2018: How momentum coupling affects SST variance and large-scale Pacific climate variability in CESM. *J. Climate*, **31**, 2927–2944, https://doi.org/10.1175/JCLI-D-17-0645.1.

Liu, Z., and E. Di Lorenzo, 2018: Mechanisms and predictability of Pacific decadal variability. *Curr. Climate Change Rep.*, **4**, 128–144, https://doi.org/10.1007/s40641-018-0090-5.

Martin, P. E., B. K. Arbic, A. M. Hogg, A. E. Kiss, J. R. Munroe, and J. R. Blundell, 2020: Frequency-domain analysis of the energy budget in an idealized coupled ocean–atmosphere model. *J. Climate*, **33**, 707–726, https://doi.org/10.1175/JCLI-D-19-0118.1.

Menary, M. B., D. L. R. Hodson, J. I. Robson, R. T. Sutton, and R. A. Wood, 2015: A mechanism of internal decadal Atlantic Ocean variability in a high-resolution coupled climate model. *J. Climate*, **28**, 7764–7785, https://doi.org/10.1175/JCLI-D-15-0106.1.

Minobe, S., A. Kuwano-Yoshida, N. Komori, S.-P. Xie, and R. J. Small, 2008: Influence of the Gulf Stream on the troposphere. *Nature*, **452**, 206–209, https://doi.org/10.1038/nature06690.

O'Rourke, A. K., B. K. Arbic, and S. M. Griffies, 2018: Frequency-domain analysis of atmospherically forced versus intrinsic ocean surface kinetic energy variability in GFDL's CM2-O model hierarchy. *J. Climate*, **31**, 1789–1810, https://doi.org/10.1175/JCLI-D-17-0024.1.

Renault, L., M. J. Molemaker, J. Gula, S. Masson, and J. C. McWilliams, 2016: Control and stabilization of the Gulf Stream by oceanic current interaction with the atmosphere. *J. Phys. Oceanogr.*, **46**, 3439–3453, https://doi.org/10.1175/JPO-D-16-0115.1.

Sérazin, G., T. Penduff, B. Barnier, J.-M. Molines, B. K. Arbic, M. Müller, and L. Terray, 2018: Inverse cascades of kinetic energy as a source of intrinsic variability: A global OGCM study. *J. Phys. Oceanogr.*, **48**, 1385–1408, https://doi.org/10.1175/JPO-D-17-0136.1.

Sheng, J., and Y. Hayashi, 1990: Observed and simulated energy cycles in the frequency domain. *J. Atmos. Sci.*, **47**, 1243–1254, https://doi.org/10.1175/1520-0469(1990)047<1243:OASECI>2.0.CO;2.

Small, R. J., and Coauthors, 2008: Air–sea interaction over ocean fronts and eddies. *Dyn. Atmos. Oceans*, **45**, 274–319, https://doi.org/10.1016/j.dynatmoce.2008.01.001.

——, F. O. Bryan, S. P. Bishop, S. Larson, and R. A. Tomas, 2020: What drives upper-ocean temperature variability in coupled climate models and observations? *J. Climate*, **33**, 577–596, https://doi.org/10.1175/JCLI-D-19-0295.1.

Smirnov, D., M. Newman, M. A. Alexander, Y.-O. Kwon, and C. Frankignoul, 2015: Investigating the local atmospheric response to a realistic shift in the Oyashio sea surface temperature front. *J. Climate*, **28**, 1126–1147, https://doi.org/10.1175/JCLI-D-14-00285.1.

Sutton, R. T., and M. R. Allen, 1997: Decadal predictability of North Atlantic sea surface temperature and climate. *Nature*, **388**, 563–567, https://doi.org/10.1038/41523.

Wilson, C., C. W. Hughes, and J. R. Blundell, 2015: Forced and intrinsic variability in the response to increased wind stress of an idealized Southern Ocean. *J. Geophys. Res. Oceans*, **120**, 113–130, https://doi.org/10.1002/2014JC010315.

Wu, L., and Z. Liu, 2005: North Atlantic decadal variability: Air–sea coupling, oceanic memory, and potential Northern Hemisphere resonance. *J. Climate*, **18**, 331–349, https://doi.org/10.1175/JCLI-3264.1.